

Effective conductivity of periodic media with cuboid inclusions

Thomas Harter *, Christen Knudby

Department of Land, Air, and Water Resources, University of California, 119 Viehmeier Hall, One Shields Ave, Davis, CA 95616, USA

Received 31 December 2003; received in revised form 14 June 2004; accepted 6 July 2004

Abstract

This paper presents a numerical solution for the effective conductivity of a periodic binary medium with cuboid inclusions located on an octahedral lattice. The problem is defined by five dimensionless geometric parameters and one dimensionless conductivity contrast parameter. The effective conductivity is determined by considering the flow through the “elementary flow domain” (EFD), which is an octant of the unitary domain of the periodic media. We derive practical bounds of interest for the six-dimensional parameter space of the EFD and numerically compute solutions at regular intervals throughout the entire bounded parameter space. A continuous solution of the effective conductivity within the limits of the simulated parameter space is then obtained via interpolation of the numerical results. Comparison to effective conductivities derived for random heterogeneous media demonstrate similarities and differences in the behavior of the effective conductivity in regular periodic (low entropy) vs. random (high entropy) media. The results define the low entropy bounds of effective conductivity in natural media, which is neither completely random nor completely periodic, over a large range of structural geometries. For aniso-probable inclusion spacing, the absolute bounds of K_{eff} for isotropic inclusions are the Wiener bounds, not the Hashin-Shtrikman bounds. For isotropic inclusion and isoprobable conditions well below the percolation threshold, the results are in agreement with the self-consistent approach. For anisotropic cuboid inclusions, or at relatively close spacing in at least one direction ($p > 0.2$) (aniso-probable conditions), the effective conductivity of the periodic media is significantly different from that found in anisotropic random binary or Gaussian media.

© 2004 Elsevier Ltd. All rights reserved.

1. Introduction

Effective properties of patterned or structured media have been the topic of many research branches in physics, engineering, and chemistry. An excellent historic review on this so-called “homogenization quest” in several fields of science is provided by Markov [33]. Other recent reviews on the topic are presented by Torquato [53] and Milton [39]. In the exploration of geofluids (groundwater, oil, gas), patterns and structures in the distribution of subsurface rock and in sediment properties provide the framework for understanding the movement of fluids and gases in a naturally heterogeneous environment [2,10]. Patterns relevant to subsurface flow

and transport can be recognized at many different scales forming a natural hierarchy [13,10] or a “scaleway” [54], which also gives rise to fractal patterns (e.g. [58,40,41,9,51]). Most hydrogeological studies focus on a specific portion of this scaleway and consider essentially two scales: the micro-scale, also referred to as the local scale [14], at which constitutive physical relationships are considered valid, and a macro-scale for which we seek to derive effective properties [34].

Structures in such media can be divided into two major groups: regular patterns and random patterns (Fig. 1). The (geo)statistical characteristics and effective properties of media with *random* patterns have been the subject of much research work in subsurface hydrodynamics (geostatistics of continuous variables, indicator geostatistics, stochastic continuum theory in subsurface hydrology and petroleum engineering, see, e.g., [29,14,15,23]). In hydrogeology and related fields, less attention

* Corresponding author. Fax: +1 530 752 5262.

E-mail addresses: thharter@ucdavis.edu (T. Harter), cjknudby@ucdavis.edu (C. Knudby).

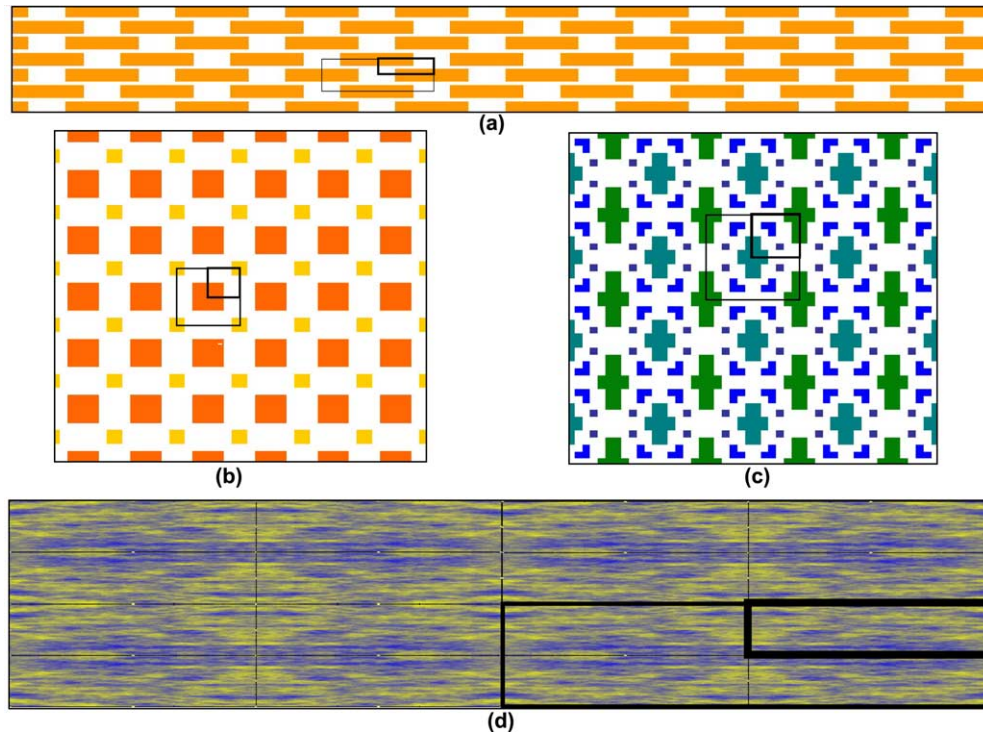


Fig. 1. Various periodic patterns in 2D: rectangular inclusions of identical size (a), square inclusions of different size (b), multiple inclusions of different size and shape (c), a realization of a stochastic “random” field arranged into a periodic pattern (d).

has been given to deterministic *regular* patterns, partly because strict regular patterns rarely occur in geologic environments. Yet, regular patterns are attractive study objects because they provide a simplified but justifiable conceptual representation that captures many salient features of random patterns [59]. Furthermore, results obtained with regular patterns can be very useful benchmarks against which approximate analytical and numerical methods as well as field results can be tested.

Regular patterns, usually referred to as periodic media within the context of homogenization [34], are defined by a “unitary domain” [46] or “unit cell” [28] that is repeated in space. The concept of periodic media is equivalent to that of stationarity (statistical homogeneity) in random media [33]. Because of its periodic nature, some effective properties of the macro-domain can be obtained by studying a single unitary domain with a simple pattern. Binary (two-phase) patterns with cuboid, spherical, or ellipsoidal inclusions (rectangles, circles, or ellipses in 2D) embedded in a homogeneous background (matrix) are perhaps the most universal and have therefore been studied most extensively.

The study of effective properties of media with circular (2D) and spherical inclusions (3D) dates back more than a century [36], but is still relevant (e.g. [63,44,16,6,21]). The use of elliptical (2D) or ellipsoidal (3D) inclusions leads to a slightly less attractive but still solvable mathematical problem (e.g. [38,37,45,32]). The

use of elliptical or ellipsoidal inclusions allow for the extension to anisotropic materials. Another type of anisotropic materials contain rectangular (2D) or cuboidal (3D) inclusions. Mathematically, this problem is considerably more involved (e.g. [43]). Effective properties of media with cubed, touching and non-touching inclusions distributed on a cubic lattice have among others recently been studied by Nozad et al. [42], Hsu et al. [27], Fisher and Stroud [22], Obsonov [43], and Fel and Kaganov [21]. Analytical models of effective conductivity in media with (2D-) rectangular inclusions arranged on a checkerboard lattice were developed by Ke-da et al. [30] and by Hui and Ke-da [26]. The specific case of touching squares in a checkerboard has been discussed, e.g., by Dykhne [20] and Yeo and Zimmerman [62].

Besides the determination of exact properties of periodic patterns, the analysis of flow around and through single inclusions have also lead to widely used formulas for effective properties of composite media containing many inclusions. These formulas are in many cases exact for periodic patterns, but are still useful approximations for statistically homogeneous irregular patterns. Examples of such upscaling formulas are the Maxwell approximation, which is valid for low inclusion concentrations, and the various effective medium theory approximations of which the self-consistent approximation is perhaps the best known in hydrogeology (e.g. [11,12,14,45]). The composite spheres assemblage, introduced by Ha-

shin and Shtrikman [25], also allows for the deduction of bounds on effective properties. It was extended to anisotropic composites by Milton [38]. Regular patterns of packed bed spheres have been used as an approximation of random media for the derivation of the classic cleaned colloid filtration model [61]. An exhaustive review of upscaling methods used in hydrogeology can be found in Renard and de Marsily [46].

In this paper, we determine the effective conductivity of binary periodic media with isotropic and anisotropic cuboid inclusions distributed on an octahedral lattice. This particular pattern has not been previously investigated, but is particularly attractive to hydrogeology due to the alternating positions of individual inclusions, which can form interlacing, non-touching patterns that are not uncommonly observed in natural media.

Determining the effective conductivity is a two-step process, which includes (1) a description of the constitutive dimensionless geometry of the unitary domain (equivalent to the geostatistical model in stochastic analysis), which we will show to include five independent parameters; and (2) a derivation of the effective conductivity. Here, we apply a conceptually simple “brute force” approach to numerically derive a general solution for the effective conductivity: We compute accurate numerical solutions for a broad range of values within the five-dimensional parametric space of the constitutive geometry and for a large range of conductivity contrasts between the two media phases. Approximate solutions throughout the continuous dimensionless parametric range are then computed by computationally inexpensive non-linear interpolation. We present significant results and compare the solution to effective conductivity estimates obtained for random heterogeneous porous media with binary and log-normal conductivity distribution and to those obtained from the self-consistent approach.

2. Methods

We refer to the isolated, mutually disconnected inclusions as the ω -phase or simply as “inclusions” and to the continuous, completely connected background phase as the η -phase [59] or simply the “matrix”. The binary medium represents the distribution of two different flow phases with conductivities K_η and K_ω , for which we seek to determine the effective conductivity under steady-state flow conditions. The constitutive equation applicable at the micro-scale (e.g., the representative elementary volume scale, [2]) is:

$$\nabla K \nabla h = 0 \quad (1)$$

subject to Ω_h and Ω_q , where K is the isotropic local conductivity, $K(x \in \Omega_\eta) = K_\eta$, $K(x \in \Omega_\omega) = K_\omega$, h is the hydraulic head or total potential, Ω_η is the matrix do-

main, Ω_ω is the domain of the inclusions, and Ω_h , Ω_q are constant head and constant flux boundary conditions, respectively, at the boundary of the macro-domain. This is the conductivity equation of composite materials, which applies equivalently to electrical conduction, thermal conduction, diffusion, dielectrics, magnetism, and antiplane elasticity [39]. To emphasize the applicability of our results to other fields, we refer to K simply as conductivity (not specifically as hydraulic conductivity).

2.1. The geometry of simple patterns in a macroscopically uniform flow field

We consider flow in binary periodic media with identically sized cuboid inclusions driven by a pressure gradient parallel to one of the cuboid axes. The inclusion centroids are distributed on an octahedral lattice, which we consider as an extension of the more common applications of a parallelepiped lattice and the equivalent 2D lattices, namely the diamond (checkerboard) and rectangular lattices, respectively (e.g., [19,60]).

The concept of the unitary domain is illustrated in Figs. 2 (2D) and 3 (3D). Due to symmetry considerations, the entire flow field through the unitary domain can be obtained by mirror-imaging the flow field from any one of the unitary domain octants (quadrants in 2D, Fig. 2). We call this cuboid octant of the unitary domain the “elementary flow domain” (EFD). Note that the EFD for a parallelepiped (rectangular) lattice contains a single inclusion in one corner (e.g., [32,1], here referred to as “Type I EFD”); The EFD for an octahedral (diamond) lattice contains two equally sized inclusions in two diagonally opposite corners (“Type II EFD”). The inclusions in the EFD each represent an octant of the cuboid inclusions in the macro-domain.

2.2. Parametrization of the constitutive geometry of cuboid inclusions

The geometry of a cuboid EFD is defined by six parameters, which all have dimensions of length: the length, d_x , width, d_y , and height, d_z , of the EFD and the length, b_x , width, b_y , and height, b_z , of the cuboid inclusion. Using the Buckingham Π theorem from dimensional analysis (c.f., [48]), it follows that the EFD geometry \mathcal{G} can be defined by five dimensionless, scale-invariant parameters, for example:

$$R_{bh} = \frac{b_y}{b_x}, \quad R_{bv} = \frac{b_z}{b_x}, \quad L_x = \frac{d_x}{b_x}, \quad L_y = \frac{d_y}{b_y}, \quad L_z = \frac{d_z}{b_z} \quad (2)$$

where the x -dimension represents the mean flow direction (direction of the macroscopic gradient), R_{bh} represents the inclusion width-to-length ratio, R_{bv} represents the inclusion height-to-length ratio, L_x represents the ra-

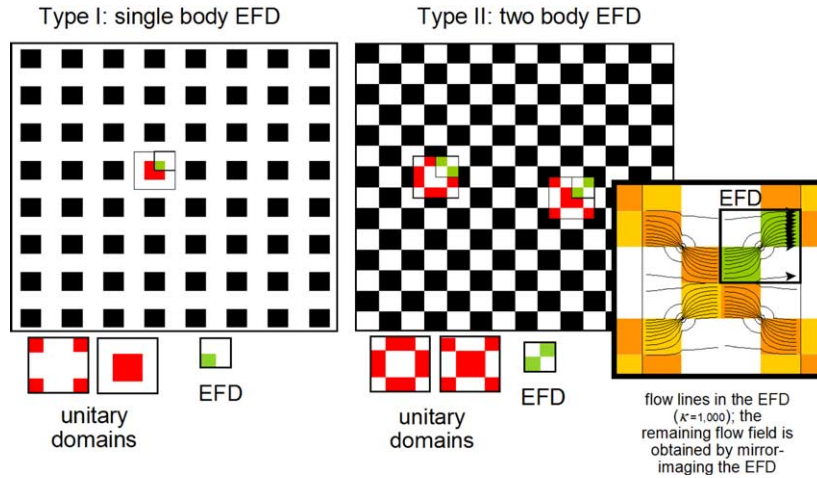


Fig. 2. Two-dimensional Type I (rectangular lattice) and Type II (hexagonal or checkerboard lattice) patterns, illustrating the relationship between the unitary domain and the macro-domain, the relationship between the elementary flow domain (EFD) and the unitary domain, example EFD flow (for $\kappa = 1000$) and the demonstration of the symmetry relationships that define the EFD within the macro-domain.

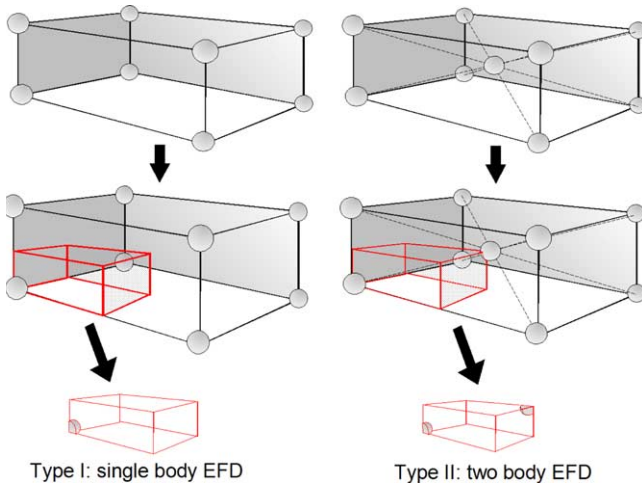


Fig. 3. Definition of the three-dimensional parallelepiped (Type I, left) and octahedral (Type II, right) lattice and illustration of the Elementary Flow Domain (EFD) with one and two one-eighth sized inclusions, respectively.

ratio of EFD length to inclusion length, L_y represents the ratio of EFD width to inclusion width, and L_z represents the ratio of EFD height to inclusion height. L_x, L_y, L_z represent the length-scale of the EFD relative to the cuboid inclusions. Other important dimensionless parameters associated with \mathcal{G} are:

$$R_{dh} = \frac{L_y}{L_x}, \quad R_{dv} = \frac{L_z}{L_x}, \quad p_1 = \frac{p_{II}}{2} = \frac{b_x b_y b_z}{d_x d_y d_z} \quad (3)$$

R_{dh} is the relative EFD width-to-length ratio; R_{dv} is the relative EFD height-to-length ratio; p is the volume proportion of the inclusions within the EFD and is equal to the proportion of inclusions within the aquifer (subscripts refer to Type I and Type II EFDs). The inclusion lengths in the EFD are half of the actual inclusion lengths in the unitary domain (Fig. 3).

Since the inclusions are, by definition, smaller than the EFD, the side-lengths of the inclusions are bounded by the side-lengths of the EFD. Hence, only three of the five dimensionless parameters in (2) can be defined arbitrarily, the fourth and fifth are bound by the choices of the first three. For example, for $R_{bh} \in]0; \infty[$ and $R_{bv} \in]0; \infty[$ and $p \in]0; 1[$, it can be shown from (2) and (3) that L_z and, given L_z , then L_y are bounded such that:

$$\text{Type I : } 1 \leq L_z \leq 1/p \quad (4a.I)$$

$$\text{then : } 1 \leq L_y \leq 1/p \cdot 1/L_z \quad (4b.I)$$

and L_x is a dependent variable :

$$L_x = 1/p \cdot 1/L_z \cdot 1/L_y \quad (4c.I)$$

$$\text{Type II : } 1 \leq L_z \leq 2/p \quad (4a.II)$$

$$\text{then : } 1 \leq L_y \leq 2/p \cdot 1/L_z \quad (4b.II)$$

and L_x is a dependent variable :

$$L_x = 2/p \cdot 1/L_z \cdot 1/L_y \quad (4c.II)$$

$$\text{subject to : } \text{Maximum}\{L_x, L_y, L_z\} \geq 2 \quad (4d.II)$$

The additional limitation (4d.II) in Type II arises from the fact that the two inclusion cuboids in the EFD cannot overlap, i.e., in at least one direction the length-scale of the EFD is greater than 2. For either geometry, if one of $\{L_x, L_y, L_z\}$ is unity, the inclusion is a collection of macroscopically sized parallel columns oriented in the $x, y,$ or z direction respectively. If any two of $\{L_x, L_y, L_z\}$ are unity, the inclusions are a collection of parallel macroscopic planes. We also note that the flow patterns for $\mathcal{G} = \{R_{bh}, R_{bv}, L_y, L_z, p\}$ are equal to the flow patterns for $\mathcal{G} = \{R_{bv}, R_{bh}, L_z, L_y, p\}$, since flow is considered to be along the x -axis and the two cases merely reflect a 90° rotation of the unitary domain around the x -axis.

2.3. Effective conductivity of EFDs with cuboid inclusions

2.3.1. Definition of K_{eff}

Due to the flow field symmetry, the EFD has no-flow boundary conditions on the faces parallel to the macroscopic hydraulic gradient, $J = \langle \nabla h \rangle$, and constant, uniform pressure heads on the two faces orthogonal to the main gradient with area $A_{\text{EFD}} [L^2]$. The pressure head difference between the two faces, $\Delta h [L]$, which are separated by $d_x [L]$ is

$$\Delta h = J \cdot d_x \quad (5)$$

By definition of the periodic boundary conditions, the effective conductivity of the macro-domain is equal to the effective conductivity of the unitary domain, and hence, equal to that of the EFD (e.g., [32]):

$$K_{\text{eff}} = (Q_{\text{macro}}/A_{\text{macro}}) \cdot J^{-1} = (Q_{\text{EFD}}/A_{\text{EFD}}) \cdot J^{-1} \quad (6)$$

$(Q_{\text{EFD}}/A_{\text{EFD}}) [L/T]$ is the total flux density through the EFD, which depends on the conductivities, K_η and K_ω , of the two materials, the shape of the EFD, and on the size and shape of the inclusions. Note that for a given \mathcal{G} , the flux density and therefore the effective conductivity is scale-invariant (independent of the actual length-scale), hence:

$$K_{\text{eff}} = f(K_\eta, K_\omega, \mathcal{G}) \quad (7)$$

for example,

$$K_{\text{eff}} = f(K_\eta, K_\omega, R_{bh}, R_{bv}, L_x, L_y, L_z) \quad (8)$$

2.3.2. Effective bounds of K_{eff}

Given p , K_η , and K_ω , the range of K_{eff} over all possible \mathcal{G} is limited by the harmonic and arithmetic mean [57]. The bounds are obtained at the one-dimensional limiting cases of the EFD geometry. When $L_y = L_z = 1$, flow is orthogonal to alternating layers of ω - and η -phases. The effective conductivity is the volume weighted harmonic mean K_H of the material conductivities:

$$1/K_{\text{eff}} = 1/K_H = p/K_\omega + (1-p)/K_\eta \quad (9)$$

When $L_x = 1$ and either $L_y = 1$ or $L_z = 1$, phases are arranged in layers parallel to mean flow. K_{eff} is given by the volume weighted arithmetic mean K_A of the material conductivities:

$$K_{\text{eff}} = K_A = p \cdot K_\omega + (1-p) \cdot K_\eta \quad (10)$$

2.3.3. Relevant parametric range for computing K_{eff}

Computing an effective conductivity is of interest primarily when the dimensionless conductivity contrast κ , $\kappa = K_\omega/K_\eta$, and the proportions of the phases, p and $(1-p)$, are such that K_A and K_H of the EFD are significantly different from each other, i.e., $\gamma \gg 1$, where

$\gamma = K_A/K_H$. Otherwise, an approximation of K_{eff} with either K_A or K_H or with the geometric mean, $K_G = 10^{(\lg K)}$, would serve many practical purposes, regardless of the arrangement of the phases within the flow domain.

Expanding the definition of γ by using equations (9) and (10) for K_A and K_H , γ can be expressed as a function of inclusion volume, p , and the conductivity contrast, κ :

$$\gamma = ap^2 - ap + 1, \quad \text{where } a = 2 - \kappa - (\kappa^{-1}) \quad (11)$$

It can be readily shown that γ is greater than a threshold, γ_0 , at given p , if κ meets the following condition:

$$(\kappa - \kappa^{-1}) > 2 + [(\gamma_0 - 1)/(p - p^2)] \quad (12)$$

and, equivalently, the volume proportions of both materials, given κ and γ_0 , are bounded by:

$$\frac{1}{2} - \sqrt{\frac{1}{4} - \frac{1 - \gamma_0}{2 - \kappa - \kappa^{-1}}} < p, \quad (13)$$

$$(1-p) < \frac{1}{2} + \sqrt{\frac{1}{4} - \frac{1 - \gamma_0}{2 - \kappa - \kappa^{-1}}}$$

If we set $\gamma_0 = 2$ and $\kappa \geq 10$, the above equation simplifies to yield a very practical rule of thumb:

A significant difference between K_H and K_A is only

$$\text{observed if both, } p \geq \kappa^{-1} \quad \text{and} \quad (1-p) \geq \kappa^{-1}. \quad (14)$$

And the corollary rule of thumb:

A significant difference between K_H and K_A is only

$$\text{observed if both, } \kappa \geq p^{-1} \quad \text{and} \quad \kappa \geq (1-p)^{-1}. \quad (15)$$

2.3.4. Computation of K_{eff}

Given \mathcal{G} , K_η , and K_ω , we obtain the effective conductivity, K_{eff} , by solving the steady-state flow equation (1) for the EFD subject to mean flow parallel to the x -axis. From the solution to (1), we can solve the momentum equation (Darcy's law) and integrate over the outflow face of the EFD to obtain the EFD flux. From (6) we then compute K_{eff} , obtain its log-transform, and normalize $\lg K_{\text{eff}}$ with respect to its Wiener bounds [57]:

$$K_{\text{eff}}^* = (\lg K_{\text{eff}} - \lg K_H) / (\lg K_A - \lg K_H) \quad (16)$$

From the Buckingham A theorem (c.f., [48]), it follows that the dimensionless effective conductivity, K_{eff}^* , which varies between 0 and 1, is a function of κ and \mathcal{G} only, but not of the actual value K_ω or K_η or the actual length scale of the EFD. A general solution for K_{eff} can therefore be obtained by considering the six-parametric space spanned by κ and \mathcal{G} .

We use a numerical procedure coupled with non-linear interpolation to obtain the general solution for $K_{\text{eff}}^*(\kappa, \mathcal{G})$:

Table 1
Parameter values used for the simulations subject to the limits (3)–(5)

R_{gh}	0.01, 0.1, 1, 10
R_{gv}	0.001, 0.01, 0.1, 1, 10, 100
L_x	1.0667, 1.3617, 1.8824, 3.0476, 8
L_y	1.0667, 1.3617, 1.8824, 3.0476, 8
L_z	1.0667, 1.3617, 1.8824, 3.0476, 8
κ	0.0001, 0.01, 0.1, 10, 100, 1000

Simulations were set up in terms of finite difference grid-block width-to-length ratio, R_{gh} , grid-block thickness-to length ratio, R_{gv} , and the number of finite difference grid-blocks per inclusion side-length. The simulation domain was set to $64 \times 64 \times 64$ grid-blocks, hence $R_{gh} = R_{dh}$ and $R_{gv} = R_{dv}$. Note that $R_{bh} = R_{gh} * L_x / L_y$ and $R_{bv} = R_{gv} * L_x / L_z$.

We define the limits of the six-dimensional parameter space $\{\kappa, R_{bh}, R_{bv}, L_x, L_y, L_z\}$ such that many practical applications for flow in porous media are included. The six-dimensional parameter space is limited by geometric considerations (Eq. (4)) and practical considerations (rule 14 or 15). From this bounded six-dimensional space, we select a finite number of regularly spaced parameter combinations with four to six values per parameter, yielding a total set of 14,114 possible parameter combinations (Table 1). For each parameter combination, we numerically solve (1) over the EFD using a grid-cell centered finite difference algorithm with a conjugate gradient solver (“MODFLOW”, [24]). The

finite difference grid spanning the EFD consists of $64 \times 64 \times 64$ grid-cells. Since the number of grid cells in each dimension is identical, the ratios of cell width and cell height to cell length is equal to R_{dh} and R_{dv} , respectively; hence, for practical reasons we defined the simulation parameter space (Table 1) in terms of R_{dh} and R_{dv} instead of R_{bh} and R_{bv} . The choice of minimum and maximum inclusion length (which define L_x, L_y , and L_z , see Table 1) are dictated by numerical considerations: Minimum thickness of each phase is set to be at least eight grid-cells or equivalent to 24 grid-cells per correlation length (see equation (18), below). This discretization is almost one order of magnitude finer than the 4 grid-cells per correlation length typically found sufficient for modeling heterogeneous porous media with binary, bimodal, or continuous conductivity distribution (e.g., [17,56]).

Here, we apply the procedure specifically for solving $K_{eff}^*(\kappa, \mathcal{G}_{II})$ (cuboids on an octahedral lattice), which is of particular interest to geologic media due to the alternating position and potential interlacing of inclusions. Solutions for the parallelepiped lattice are provided, e.g., by Lu [32] who specifically considered spheroidal inclusions. To obtain a continuous solution $K_{eff}^*(\kappa, \mathcal{G}_{II})$ from the individual simulations, we map $K_{eff}^*(\kappa, \mathcal{G}_{II})$ by non-linear interpolation within the parameter range

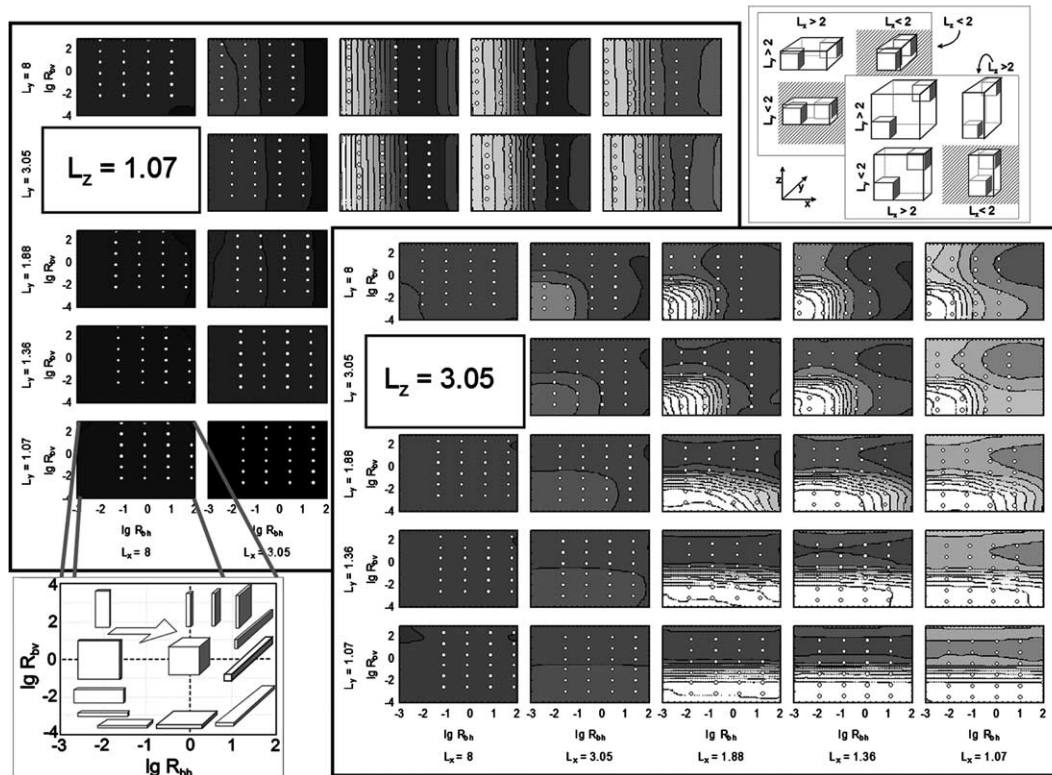


Fig. 4. Illustration of the dependence of effective conductivity, K_{eff}^* , on geometric structure in a strongly heterogeneous periodic media with high conductivity inclusions ($\kappa = 1,000$). Values in the grayscale maps of K_{eff}^* vary from approximately 0 (black) to approximately 1 (white). In the lower left corner, the insert illustrates the inclusion shapes represented by the map region $\{lg R_{bh}, lg R_{bv}\}$. In the upper right corner, the insert illustrates the inclusion arrangements within the EFD as represented by the respective maps in the two panels.

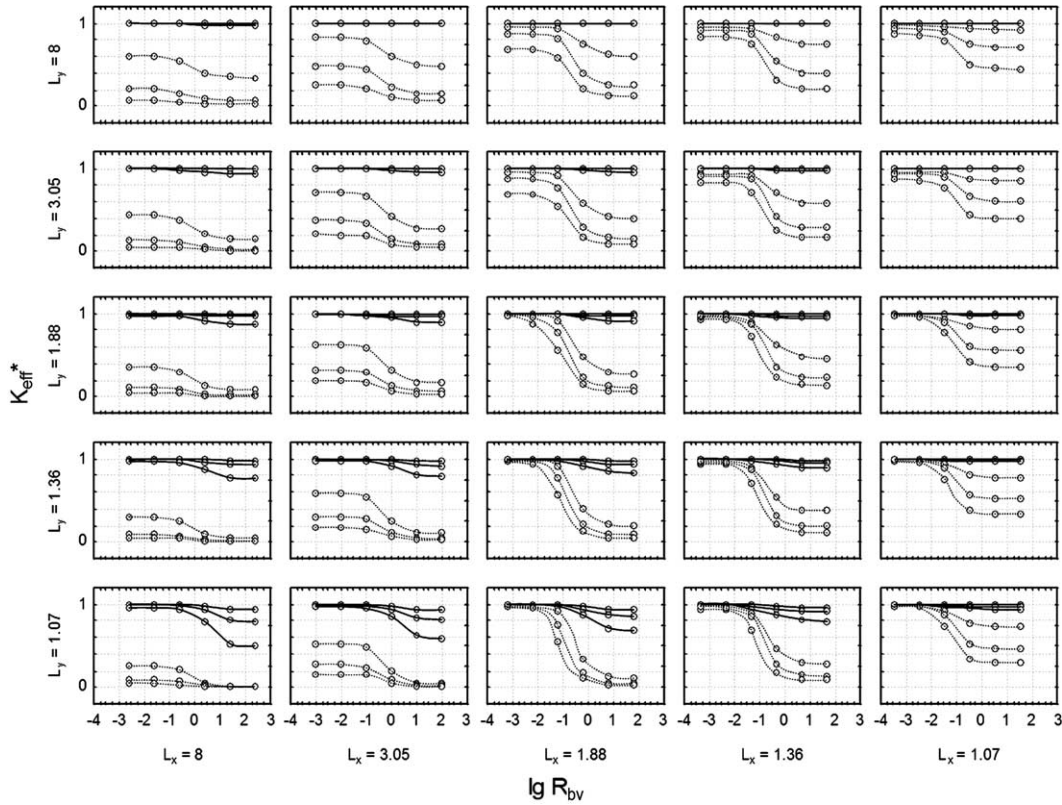


Fig. 5. Univariate results of $K_{\text{eff}}^*(R_{bv})$ for $\lg R_{bh} < 0$ and the same combinations of $\{L_x, L_y\}$ as the right panel of Fig. 4 ($L_z = 3.05$). The sets of six curves in each graph are for (from top to bottom) $\kappa = 0.0001, 0.01, 0.1, 10, 100, 1000$.

used for the computations (Table 1). Maps of $K_{\text{eff}}^*(\kappa, \mathcal{G}_{\text{II}})$ shown in Fig. 4 are obtained by distance-weighted least square estimation of K_{eff}^* on a 30×30 point grid given measured K_{eff}^* values on the 5×5 ($\lg R_{bh}, \lg R_{bv}$) datapoints shown. The estimation procedure is a polynomial (second-order) regression, whereby the weight decreases with distance from the measured datapoints ($R_{bh}, R_{bv}, K_{\text{eff}}^*$) [35,52]. In the univariate examples of K_{eff}^* shown in Figs. 5–8, we use graphical interpolation.

3. Results

3.1. Patterns in \mathcal{G}_{II}

To understand the behavior of $K_{\text{eff}}^*(\kappa, \mathcal{G}_{\text{II}})$, we first consider the geometric patterns generated by $\mathcal{G}_{\text{II}} = \{R_{bh}, R_{bv}, L_x, L_y, L_z\}$. The first two parameters R_{bh} and R_{bv} describe the eccentricity or anisotropy of the cuboid inclusions, which can be divided into three categories (Fig. 4, lower left insert):

- isotropic, cubic or near-cubic: ($R_{bh} \sim R_{bv} \sim 1$)
- anisotropic, planar:
 - parallel to the mean flow direction: $R_{bv} \ll 1$ (horizontal) or $R_{bh} \ll 1$ (vertical)

- orthogonal to the mean flow direction: $R_{bh} \gg 1$ and $R_{bv} \gg 1$ (vertical)
- anisotropic, columnar:
 - parallel to the mean flow direction: ($R_{bh} \sim R_{bv} \ll 1$)
 - orthogonal to the mean flow direction: $R_{bh} \sim 1$ and $R_{bv} \gg 1$ (vertical) or vice versa (horizontal).

The three parameters L_x, L_y, L_z describe the spacing of the inclusions in each direction and also define the total volumetric proportion p of the ω -phase. Since L_x, L_y, L_z are dimensionless measures of EFD length, each of them is also a measure of the directional proportion of the ω -phase material. If the relative spacing is not equal in all three principal directions, that is, if either $R_{dh} \neq 1$ or $R_{dv} \neq 1$ or both, the probability to encounter the ω -phase along a straight line is not independent of the direction of that line. The existence of an inequality between L_i and $L_j, i, j \in \{x, y, z\}$ is referred to as aniso-probability. Lu [32], for example, discussed effects of aniso-probability within the context of parallelepiped array aspect ratio (i.e., R_{dh}, R_{dv}) and inclusion aspect ratio (i.e., R_{bh}, R_{bv}).

A geometric arrangement that is unique to the octahedral (as opposed to the parallelepiped) lattice is “interlacing”. Interlacing or overlapping patterns of inclusions occur if two $L_i, L_j, i, j \in \{x, y, z\}$ are smaller

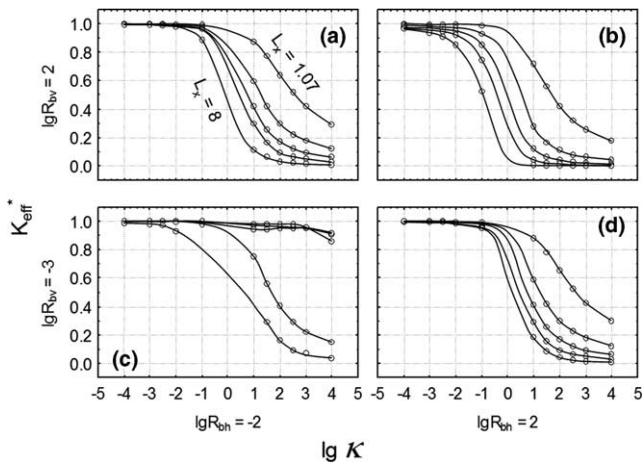


Fig. 6. Univariate results of $K_{\text{eff}}^*(\kappa)$ for $L_y = L_z = 3.05$ and four inclusion shapes $\{\lg R_{bh}, \lg R_{bv}\}$ corresponding to the near corner regions of the $\{\lg R_{bh}, \lg R_{bv}\}$ maps in Fig. 4. The sets of five curves in each graph are for (from top to bottom) $L_x = 1.07, 1.36, 1.88, 3.05, 8$.

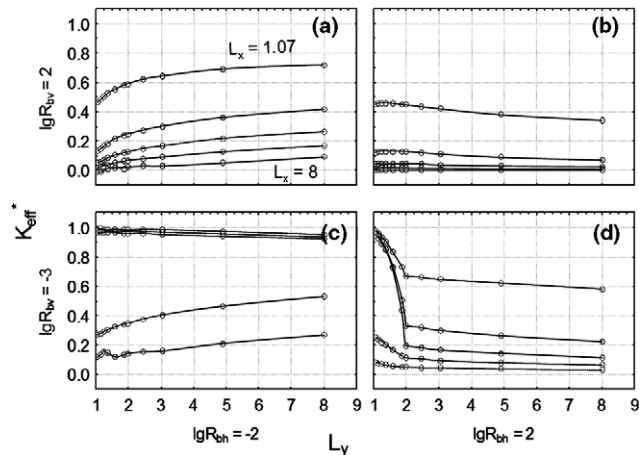


Fig. 7. Univariate results of $K_{\text{eff}}^*(L_y)$ for $L_z = 3.05$, $\kappa = 100$, and four inclusion shapes $\{\lg R_{bh}, \lg R_{bv}\}$ corresponding to the near corner regions of the $\{\lg R_{bh}, \lg R_{bv}\}$ maps in Fig. 4. The sets of five curves in each graph are for (from top to bottom) $L_x = 1.07, 1.36, 1.88, 3.05, 8$.

than 2. In that case, the third $L_k, k \in \{x, y, z\}$, must be greater than 2 (Eq. (4d.II)). Interlacing may occur parallel to the mean flow direction ($L_x < 2$, Fig. 4, upper right insert, shaded area top and right) or orthogonal to the mean flow direction ($L_x > 2$, Fig. 4, upper right insert, shaded area on the left). Interlacing occurs due to the octahedral lattice arrangement of the inclusions represented by the Type II EFD (Fig. 3). It does not occur in a parallelepiped lattice (Type I EFD) arrangement.

3.2. Effective conductivity dependence on EFD geometry and conductivity contrast

To illustrate the behavior of K_{eff}^* with \mathcal{G}_{II} , Fig. 4 shows maps of $K_{\text{eff}}^*(\lg R_{bh}, \lg R_{bv})$ in a medium with relatively high hydraulic conductivity inclusions

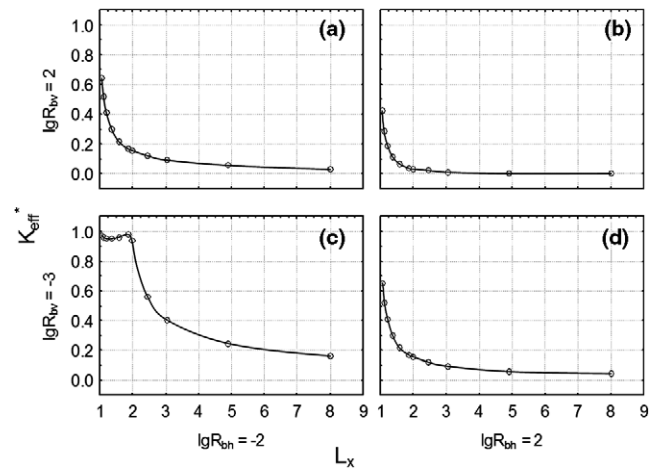


Fig. 8. Univariate results of $K_{\text{eff}}^*(L_x)$ for $L_y = L_z = 3.05$, $\kappa = 100$, and four inclusion shapes $\lg R_{bh}, \lg R_{bv}$ corresponding to the near corner regions of the $\{\lg R_{bh}, \lg R_{bv}\}$ maps in Fig. 4.

($\kappa = 1000$). Each map spans the entire simulated range of $\lg R_{bh}, \lg R_{bv}$. The two-dimensional space within each map represents various inclusion shapes (schematically illustrated in the lower left corner insert). Maps are shown for L_z just above 1 (upper left panel of maps) and for $L_z \sim 3$ (lower right panel of maps). Each of the two panels shows various maps, each for a specific combination of L_x and L_y . Corresponding inclusion arrangements of $\{L_x, L_y, L_z\}$ are schematically illustrated in the upper right hand insert of Fig. 4 using a cubic inclusion example. No solutions exist for L_x, L_y , and L_z being smaller than 2 (area of the left panel covered by the right panel) (Eq. (4d.II)). The grayscale maps of K_{eff}^* vary from 0 (black) to 1 (white) indicating whether the actual effective conductivity, K_{eff} , is close to either the harmonic mean conductivity (black) or to the arithmetic mean conductivity (white), or in between (gray). Figs. 5–8 present corresponding sets of univariate solutions of K_{eff}^* for a quantitative illustration of the behavior of $K_{\text{eff}}^*(\kappa, \mathcal{G}_{\text{II}})$.

3.2.1. Dependence on inclusion shape and conductivity contrast

The extreme values of K_{eff}^* within a map (within the range of simulated R_{bh} and R_{bv}) always occur at the map fringe. This means that the most eccentrically shaped inclusions yield the lowest and highest K_{eff}^* . Values of K_{eff}^* monotonically increase or decrease along the x - and y -direction of the mapped area. The highest K_{eff}^* —if there are significant variations at all—are always observed in the lower left map area ($R_{bh} \ll 1$ and $R_{bv} \ll 1$), which represents columnar or planar inclusions whose main eccentricity axis is oriented parallel to the mean flow direction (longitudinal inclusions, see lower left cartoon, Fig. 4). This behavior arises because, given a specific volumetric proportion p of the inclu-

sions, longitudinal inclusions provide the most continuity along the flow direction. This is true regardless of the magnitude of κ (Fig. 5): for $\kappa > 1$, longitudinal inclusions provide relatively longer flow-path lengths within high conductivity inclusions than transverse inclusions. For $\kappa < 1$, longitudinal inclusions provide the least resistance to flow in the high conductivity matrix.

The lowest K_{eff}^* always occurs in the upper right map area ($R_{bh} \gg 1$ and $R_{bv} \gg 1$), which represents planar inclusions that are oriented orthogonal across the mean flow direction. Regardless of κ , the perpendicular orientation of the planar inclusions minimizes the longitudinal continuity of the flow paths and, hence, minimizes the effective conductivity (e.g., [31]). In the subsurface, such conditions are often encountered in vertical flow through aquitards, which occurs across the main direction of hydrostratigraphic layering; and in fractured rock where the macroscopic hydraulic gradient is perpendicular to the orientation of the main fracture bedding plane.

Another distinct feature of the maps in Fig. 4 is that the largest rate of change in $K_{\text{eff}}^*(\lg R_{bh}, \lg R_{bv})$ always occurs near the central map portion ($R_{bh} \sim R_{bv} \sim 1$). From a physical point of view, this means that the effective conductivity is most sensitive to the cuboid inclusion shape if the inclusions have low eccentricity. The univariate functions $K_{\text{eff}}^*(\lg R_{bv})$ shown in Fig. 5 provide a more quantitative interpretation of these results. To plot the univariate functions in Fig. 5, “cross-sections” along $\lg R_{bv}$ were prepared from the right-hand panel of Fig. 4 ($L_z = 3.05$) for $\lg R_{bh} < 0$ ($\lg R_{dh} = -1$, Table 1).

Fig. 5 suggests that $K_{\text{eff}}^*(\lg R_{bv})$ approximately follows a hyperbolic tangent function (not shown),

$$K_{\text{eff}}^* = a + b \cdot [1 + \tanh(-c \cdot \lg R_{bv} + d)]/2 \quad (17)$$

The coefficients, a , b , c and d are measures of the upper ($a + b$) and lower (a) asymptote of $K_{\text{eff}}^*(\lg R_{bv})$ in the limits $\lg R_{bv} \rightarrow -\infty$ and $\lg R_{bv} \rightarrow +\infty$ respectively. The parameter c is a measure of the slope in the transition from upper to lower asymptotic value, while d is a measure of the $\lg R_{bv}$ value at which $K_{\text{eff}}^*(\lg R_{bv})$ obtains the central value between the two asymptotic limits. Curves for $K_{\text{eff}}^*(\lg R_{bh})$ exhibit an equivalent functional form. However, results such as those in Fig. 5 indicate that if one were to fit (17) to the data, each of these four measures would also depend non-linearly on the remaining four geometric parameters in \mathcal{G}_{II} as well as on the conductivity contrast κ . For example, at higher L_y , a increases, albeit at different (and sometimes negligible) rates for different L_x and κ , while b decreases. The opposite occurs with increasing L_x .

The hydraulic conductivity contrast κ has significant effects on $K_{\text{eff}}^*(\lg R_{bv})$ and, equivalently, on $K_{\text{eff}}^*(\lg R_{bh})$ (not shown in Fig. 5). Most generally, for any \mathcal{G}_{II} , K_{eff}^* is found to increase with decreasing κ and vice versa, consistent, for example, with analytical results in paral-

lelepipiped lattices with spheroid inclusions [32]. When plotting the univariate function $K_{\text{eff}}^*(\lg \kappa)$ at a given \mathcal{G}_{II} , we find that the functional form of $K_{\text{eff}}^*(\lg \kappa)$ is again similar to (17) with $\lg \kappa$ replacing $\lg R_{bv}$ (Fig. 6). In most cases, the steepest decline (highest sensitivity) of $K_{\text{eff}}^*(\lg \kappa)$ occurs near $\lg \kappa = 0$, i.e., in the limit as the binary medium becomes homogeneous, where $K_{\text{eff}} = K_A = K_H$. The dimensionless $K_{\text{eff}}^*(\lg \kappa = 0)$ is indeterminate (16). However, Fig. 6 suggests that the limit of $K_{\text{eff}}^*(\lg \kappa)$ at $\lg \kappa = -0$ is identical to the limit of $K_{\text{eff}}^*(\kappa)$ at $\lg \kappa = +0$. Numerical evaluation of these limits for K_{eff}^* is limited by the accuracy of computing K_{eff}^* from K_{eff} for small values of κ . Depending on p , numerical errors in the evaluation of (16) typically become significant at $|\lg \kappa|$ smaller than 0.5–1 (see Eq. (12)).

Note that the four graphs of Fig. 6 (also Figs. 7 and 8) correspond to geometric conditions near the corresponding four map corners in Fig. 4, hence Fig. 6 shows $K_{\text{eff}}^*(\lg \kappa)$ solutions of the four most eccentric inclusion shapes, $\{R_{bh}, R_{bv}\}$, that were simulated (compare to lower left cartoon in Fig. 4). In contrast to $K_{\text{eff}}^*(\lg R_{bv})$, the parametric measures a and b of (17) for $K_{\text{eff}}^*(\lg \kappa)$ qualitatively appear to be independent of the inclusion shape and equal to 0 and 1, respectively. In other words, regardless of p , the relative effective conductivity appears to always be close to either the arithmetic mean (if $\kappa < 1$) or the harmonic mean (if $\kappa > 1$) if the conductivity contrast, $|\lg \kappa|$, is large enough. This would be consistent with results, e.g., by Hui and Ke-da [26] for a checkerboard geometry.

The inclusion shape and spacing significantly affects the spreading measure c and the offset measure d of (17) when applied to $K_{\text{eff}}^*(\lg \kappa)$. Longitudinal inclusions have the highest d values (offset to the right). As a result, for highly longitudinal inclusions (Fig. 6c), the simulations give only the left most portion of the (assumed) hyperbolic tangent function. Transverse inclusions move the offset to the left with the left-most offset (lowest d) and therefore lowest K_{eff}^* observed for planar inclusions perpendicular to the flow direction (Fig. 6b). For media with $\kappa < 1$, strong deviation from high K_{eff}^* occurs only when transverse planar inclusions interlace across the mean flow direction ($L_x > 2$). In geologic media, those conditions are often encountered in vertical flow through aquitards with well-connected inclusions of high conductivity material; on a regional scale in closed basins with thick, semi-confined aquifers that are recharged through precipitation or irrigation returns at the water table and pumped from significant depths; and in fractured rock where the macroscopic hydraulic gradient is perpendicular to the orientation of the fracture bedding plane, but where fractures are well connected.

3.2.2. Dependence on inclusion spacing

The sensitivity of K_{eff}^* on the transverse inclusion spacings, L_y and L_z is most apparent for EFDs that

contain planar inclusions oriented parallel to the mean flow direction, but whose main eccentricity axis is either vertical (Fig. 4, upper left area of each map) or horizontal across the mean flow direction (lower right area of each map): When such inclusions are closely spaced in the y -direction, i.e., $L_y < 2$, K_{eff}^* is high if the main axis of such planar inclusions is also parallel to the y -axis. In that case, K_{eff}^* becomes nearly independent of $\lg R_{bh}$ and highest K_{eff}^* are observed throughout the lower map area. Conversely, the same holds true for small vertical spacing, i.e., $L_z < 2$, and vertical (planar) inclusions. The strong interaction between K_{eff}^* and L_y for y -directional, horizontal planar inclusions leads to a particular form of $K_{\text{eff}}^*(L_y)$ (Fig. 7d): If interlacing occurs parallel to the flow direction ($L_y < 2$ and $L_x < 2$), then K_{eff}^* is very sensitive to L_y (steep slope). At $L_y \sim 2$ (limit of interlacing) and above, this interaction abruptly stops resulting in a sudden slope change in $K_{\text{eff}}^*(L_y)$. The same behavior is not observed as strongly at $L_x > 2$ (lower two curves in Fig. 7d). As a result of such geometric interactions between inclusion shape and spacing in the transverse direction, the univariate behavior of $K_{\text{eff}}^*(L_y)$ or $K_{\text{eff}}^*(L_z)$ is not always strictly monotonic and the functional form of $K_{\text{eff}}^*(L_y)$ or $K_{\text{eff}}^*(L_z)$ depends strongly on the inclusion shape (R_{bh} , R_{bv}) (Fig. 7).

Longitudinal to the mean flow direction, larger inclusion spacing generally results in lower effective conductivity (Fig. 8). With some exceptions, $K_{\text{eff}}^*(L_x)$ decreases nearly exponentially to an asymptotic base value that depends on other parameters as well (Fig. 8). Highest K_{eff}^* occur as L_x approaches 1 (Figs. 4 and 8). The near-exponential decrease is not observed for longitudinal, highly eccentric inclusions that are closely spaced (e.g., Fig. 8c). In those cases, $K_{\text{eff}}^*(L_x)$ remains uniformly high until a threshold is reached near $L_x = 2$. In dilute media, where inclusion spacing is large in all dimensions ($L_x \gg 3$ and $L_y \gg 3$ and $L_z \gg 3$; $p \ll 0.1$), K_{eff}^* is always either near 0 (high conductivity inclusions) or remains near 1 (low conductivity inclusions).

To provide an efficient continuous approximation of $K_{\text{eff}}^*(\kappa, \mathcal{G}_{\text{II}})$, a neural network was trained and tested on the empirically obtained dataset in lieu of determining a non-linear multivariate regression equation. The trained neural network represents an empirical, but universal transfer function $K_{\text{eff}}^*(\kappa, \mathcal{G}_{\text{II}})$ within the parametric bounds defined by the numerical experiment. The neural network modeling approach is described in Appendix A. A Microsoft DOS/WINDOWS program for computing $K_{\text{eff}}^*(\kappa, \mathcal{G}_{\text{II}})$ is available from the corresponding author.

4. Discussion: comparison to effective conductivity in random and self-consistent media

In subsurface hydrology, most recent work related to effective conductivity has focused on random fields, since

natural media do not exhibit the strict order of the periodic media considered here. However, the distinct occurrence of, e.g., geologic or soil “layers”, “inclusions”, etc. in natural geologic media suggests that natural media are neither completely random and complex (high entropy) nor strictly regular with simple patterns (low entropy). Similar to the Hashin-Shtrikman bounds for binary composite spheres assemblages [25], the solution described in the previous section (and encoded in the transfer function model described in Appendix A) therefore provides a low entropy bound for the effective conductivity of natural systems that is of potentially significant practical interest. We therefore focus the discussion on exploring the relationship between the parameters of the EFD and those of random fields, and on exploring similarities and differences between the effective conductivity of the Type II periodic media presented here and various random field and self-consistent representations, following the spirit of, e.g., [6].

4.1. Relationship between parameters of regular and random field geometries

The five dimensionless parameters of the EFD geometry represent the degree of anisotropy, aniso-probability, and the volume proportion of the inclusions. They are obtained by measuring the three directional mean lengths and three directional proportions of inclusions in natural media. In contrast, random binary media inclusions are often conceptualized as lacking both, order and aniso-probability. For example, indicator (“IR”) random fields [7,17,18] and transition probability-Markov chain (“TP”) random fields [7,8] assume that the mean separation distance between inclusions is isotropic, $\langle L_x \rangle = \langle L_y \rangle = \langle L_z \rangle$, and therefore entirely determined by p . Such random binary media patterns are defined by only three dimensionless parameters: the volume proportion, p , of the inclusions, and the mean anisotropy ratios, $\langle R_{bh} \rangle$ and $\langle R_{bv} \rangle$, of the random ω -phase shape. Furthermore, the ω -phase of random media does not necessarily have to be an inclusion, i.e., there is no strict isolation of the ω -phase, which results in percolation effects [50]. In both, the IR or TP random fields, the inclusion shapes are defined by their mean length l in each principal direction, and—in TP media with more than two phases—the juxtapositional preference between the sequence of phases (providing for a control of the degree of order in the random distribution of different geologic facies). The mean length ℓ of the ω -phase in IR or TP binary media is directly related to the correlation length λ of its variogram [8]:

$$\lambda_i = 3\ell_{\eta,i}(1 - p_{\eta}) \quad i = x, y, z \quad (18)$$

This relationship is useful to define equivalent parameters for regular media representations given the commonly measured variogram of geologic media.

In the limit as the number of materials becomes infinite, the distribution of material properties (e.g., conductivity) is continuous instead of discrete. In subsurface hydrology, these type of random fields are commonly modeled using a joint Gaussian probability distribution for $\lg K$ (c.f. [14]). The Gaussian random field is defined by the mean and variance of $\lg K$ (equivalent to defining proportions of phases and their conductivity contrasts) and by a covariance or variogram function with directional correlation lengths λ_i (defining the degree of anisotropy in the $\lg K$ random field).

In summary, key differences between the binary periodic media considered here and the heterogeneous random porous media typically considered in stochastic upscaling, are (1) the degree of order in the regular media, which prevents connectivity of inclusions even at a high degree of interlacing, i.e., at high p , (2) the flexibility to model anisoprobable inclusion spacing, and (3) the lack of variability in the length of individual inclusions. The next section explores to which degree these differences affect the behavior of the effective conductivity.

4.2. Comparison to effective conductivity in binary random fields

Desbarats [17] numerically computes effective conductivities of binary sand-shale sequences generated as indicator random fields. The three constitutive random field parameters are $K_{\text{sand}}/K_{\text{shale}}$, λ_z/λ_x (λ_y/λ_x is set to 1), and the volume proportions $p_{\text{shale}} = 1 - p_{\text{sand}}$. Equivalent periodic media parameters are obtained using (18), $\ell_{\eta_i}/\ell_{\eta_j} = \lambda_i/\lambda_j$, $i, j \in \{x, y, z\}$:

$$\kappa = K_{\text{sand}}/K_{\text{shale}}, \quad R_{bh} = \lambda_y/\lambda_x = 1, \quad R_{bv} = \lambda_z/\lambda_x,$$

$$L_x = L_y = L_z = [2/(1 - p_{\text{shale}})]^{1/3} \quad \text{for } p_{\text{shale}} > 0.75$$

$$\kappa = K_{\text{shale}}/K_{\text{sand}}, \quad R_{bh} = \lambda_y/\lambda_x = 1, \quad R_{bv} = \lambda_z/\lambda_x,$$

$$L_x = L_y = L_z = [2/p_{\text{shale}}]^{1/3} \quad \text{for } p_{\text{shale}} < 0.25$$

The largest L_x used in our simulation that also fulfills the iso-probability condition of the IR field is $L_x = L_y = L_z = 3$, hence $p_{\text{shale}} \leq 7.4\%$ or $p_{\text{shale}} \geq 92.6\%$, depending on whether shale is in the inclusion or in the matrix, respectively. This limits the range of comparison to extreme cases only. To allow for a comparison across a broader range of p_{shale} , we also compared the random field solutions to regular media cases with interlacing inclusions at relatively close lateral spacing: Given p , we set $L_i = 3$, and compute $L_j = L_k$, where $i, j, k \in \{x, y, z\}$, $i \neq j, k$, from Eq. (4c.II). With $L_i = 3$, inclusions begin to interlace at $p > 0.167$. At $p = 0.58$ (largest simulated value), the inclusions interlace almost completely ($L_j = L_k = 1.067$). Two main scenarios are distinguished with respect to interlacing: By setting either L_z or L_y to 3, the matrix remains open along

the mean flow (x) direction (“X-x-1” in Fig. 9, where X and x are placeholders for symbols explained below), whereas at $L_x = 3$ the inclusions interlace orthogonal to the x -direction (“X-x-2” in Fig. 9).

In infinite indicator random media, isolated phases exist only below the percolation threshold, p_c . For three-dimensional, correlated random media, $p_c \sim 13\%$ [47]. Hence, at $p_{\text{shale}} < 13\%$, shale is the isolated phase; at $p_{\text{shale}} > 87\%$, sand is the isolated phase of the IR media. At p_{shale} between 13% and 87%, both sand/sandstone and clay/shale phases are continuous, although small isolated regions of one or the other may occur.

In the periodic media, due to the isolation of the ω -phase, the solution $K_{\text{eff}}(p_{\text{shale}})$, is not unique and two sets of curves exist (Fig. 9): $\kappa < 1$ (clay/shale as inclusion, “C-x-x”, $p_{\text{shale}} < 58\%$) and $\kappa > 1$ (sand/sandstone as inclusion, “S-x-x”, $p_{\text{shale}} > 42\%$). As a result, while the effective conductivity in random binary media continuously decreases with increasing p_{shale} , the two set of curves for the periodic media (“C-x-x” vs. “S-x-x”) are distinct and disconnected: with clay/shale as inclusion (“C-x-x”), effective conductivity is much higher than with sand/sandstone as inclusion (“S-x-x”). For anisotropic and isotropic media alike and across the entire p_{shale} range, the random indicator media yields a K_{eff} that is larger than K_{eff} for “S-x-x”, but smaller than K_{eff} for “C-x-x”. This confirms that the ordered media cases provide low entropy bounds for natural media.

The influence of interlacing, at $0.16 < p < 0.58$, is significant and best observed for isotropic inclusions ($R_{bh} = R_{bv} = \lambda_z/\lambda_x = 1$): For interlacing clay/shale inclusions (“C-i-x” in Fig. 9), the effect increases with the degree of interlacing and hence with p_{shale} . Significantly lower K_{eff} are observed for interlacing perpendicular to the mean flow direction (“C-i-2”), than parallel to the mean flow direction (“C-i-1”). In the latter case, flow path tortuosity through the sand matrix (where most of the flow occurs) is much smaller. Yet, even for “C-i-2”, the effective conductivity is equal to or only slightly higher than in the isotropic random indicator media. This suggests that the periodic interlacing of low-conductivity inclusions across the mean flow path may be a practical approximation of isotropic random medium with no more than 60% clay/shale. A similar effect is observed with sand/sandstone inclusions (“S-i-x” in Fig. 9), even though the flow pattern now focuses on the inclusions: again, interlacing along the mean flow direction allows for more efficient water flow than interlacing across the mean flow direction (“S-i-1” > “S-i-2”, Fig. 9).

At low $p_{\text{sand}} < 0.16$ ($p_{\text{shale}} > 0.84$) isotropic periodic media has significantly lower K_{eff} than the isotropic random indicator media, despite the fact that sand-regions are isolated in both, the periodic and the random media. This phenomenon, also observed by Byström [6], may be explained by considering that the randomness in the

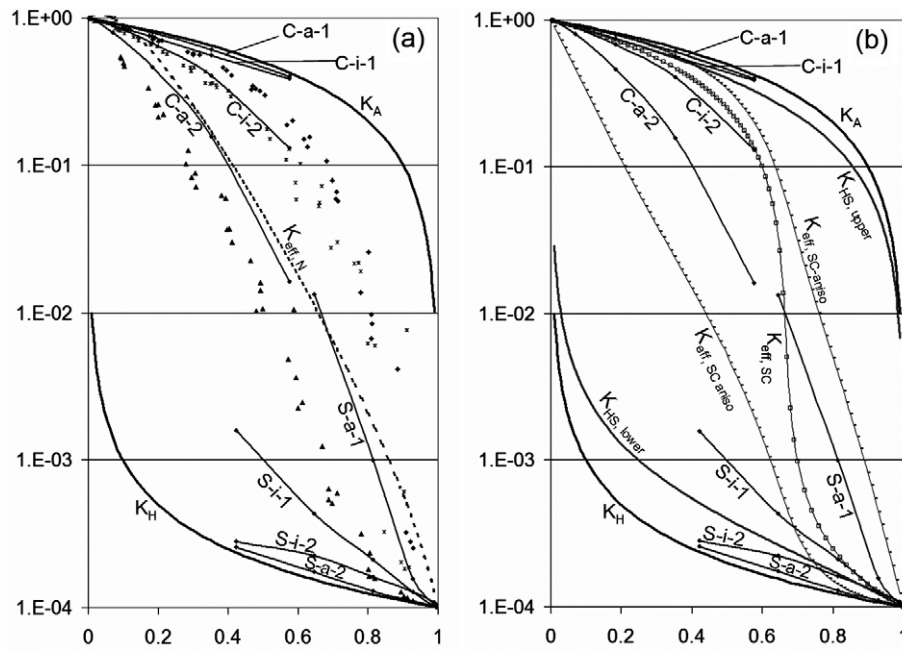


Fig. 9. K_{eff} (vertical axis) as a function of the proportion p (horizontal axis) of the low conductivity phase (shale, clay). (a) Comparison of periodic media effective conductivity to random media effective conductivity, where $\kappa = 1\text{E}-04$ (all labels “C-x-x”) and $\kappa = 1\text{E}+04$ (all labels “S-x-x”). Periodic media inclusions are isometric cubes (“X-i-x”) or (anisotropic) planar squared cuboids (“X-a-x”) with a thickness to body ratio of 1:15. The latter are oriented either parallel to the flow direction (“X-x-1”) or perpendicular to the flow direction (“X-x-2”). The inclusions are interlacing along the flow direction (“X-x-1”: $L_z = 3$) or interlacing perpendicular to the flow direction (“X-x-2”: $L_x = 3$). The effective conductivity of binary random indicator media [17] are shown by symbols: (\blacktriangle) $\lambda_z/\lambda_x = 15$, ($*$) $\lambda_z/\lambda_x = 1$, (\blacksquare) $\lambda_z/\lambda_x = 1/15$. Also shown are the effective conductivity, K_N , of isotropic Gaussian random fields, and the Wiener bounds, K_H and K_A . (b) Comparison of the periodic media effective conductivity to the effective conductivity, K_{SC} , of the self-consistent approach for isotropic media [14]; the self-consistent anisotropic (1:15 and 15:1) effective conductivities, $K_{\text{eff,SC-aniso}}$ from Poley [45]; the lower and upper Hashin-Shtrikman bounds for isotropic binary media, $K_{\text{HS,lower}}$ and $K_{\text{HS,upper}}$ [25,14]; and the Wiener bounds, K_H and K_A .

sand-region distribution of the indicator random field allows for locally closer spacing between individual sand-regions offering a shorter flow-path through the matrix and, hence, less resistance between isolated sand-regions than in the periodic media. Lateral transport within the randomly shaped sand-regions compensates for the random distribution of the shortest sand-to-sand flowpaths within the low permeable matrix. Hence, media with randomly distributed isolated sand-regions are a more efficient conductor than those with regularly distributed sand-regions. In contrast, at low p_{shale} ($p_{\text{shale}} < 0.16$, $\kappa < 1$), the effective conductivity of both the periodic and the random isotropic binary media are identical and near the arithmetic mean (Fig. 9).

The overall effect of anisotropy on K_{eff} (relative to isotropic conditions) is similar in periodic and random media (Fig. 9): Relative to isotropic media, larger K_{eff} are observed for flow parallel to layering, $\lambda_z/\lambda_x < 1$ and lower K_{eff} are observed for flow orthogonal to layering, $\lambda_z/\lambda_x > 1$. However, in periodic media, the effects of anisotropy can be further enhanced by the effects of interlacing, if interlacing is in the same direction as the main anisotropy axis. As described earlier, such ordered interlacing combined with anisotropy leads to K_{eff} being near the harmonic mean (sand/sandstone inclusions,

$\kappa > 1$) or near the arithmetic mean (clay/shale inclusions, $\kappa < 1$) across a wide range of p_{shale} or p_{sand} . In contrast, random binary media exhibits such proximity of K_{eff} to K_A or K_H only if the volumetric proportion of the inclusions is small.

4.3. Comparison to effective conductivity in Gaussian random fields

Effective conductivity, $K_{\text{eff,N}}$, of jointly normal (Gaussian) random fields have been estimated using various stochastic methods (c.f. [14]). To first order, $K_{\text{eff,N}}$ of isotropic random Gaussian media is given by:

$$K_{\text{eff,N}} = K_G [1 + \sigma_{\ln K}^2 / 6] \quad (19)$$

where K_G is the geometric mean of K and ‘ln’ is the natural logarithm. From the definition of the variance of $\ln K$, $\sigma_{\ln K}^2 = \langle (\ln K)^2 \rangle - \langle \ln K \rangle^2$, it can be shown that in binary media:

$$\sigma_{\ln K}^2 = (\ln \kappa)^2 [p(1-p)] \quad (20)$$

Inserting (20) into (19) yields a first order approximation of the effective conductivity in isotropic periodic or indicator random media. Again, comparison of ordered media effective conductivity to (19) is limited to a \mathcal{G}_{II} cu-

void periodic media approximation of a log-normal K random field bounded by the condition $L_x \sim L_y \sim L_z$ due to the assumed stationarity of the mean and variance in all three principal directions (see above). Furthermore, the Gaussian approximation applies only to $\kappa > 1$, that is $p_{\text{sand}} < p_{\text{shale}}$, since the derivation of (19) assumes a right-skewed distribution of K . The ordered media estimates of K_{eff} (“S-i-1” and “S-i-2”) are significantly lower than those for a Gaussian random field with equivalent variance. While some of the difference stems from the error incurred by applying the small variance approximation (19) to a large variance case, we observe similar differences at $\kappa = 10$, for which $\sigma_{\ln K}^2(p) < 1.3$ (not shown). Hence, equivalent to binary random fields, Gaussian random field approximations of natural random systems yield higher effective conductivity than ordered media approximations of natural random systems, thought to be due to the percolation effects caused by the random arrangement of the conductivity field (e.g., [6]).

4.4. Comparison to self-consistent approximation of effective conductivity

An analytical equation of effective conductivity based on the self-consistent approximation by Bruggeman [5] has been summarized by Beran [3] and Dagan [14]. The advantage of the approximation is that it does not assume any underlying K distribution and is not limited to small variances. For the specific case of isotropic, binary media, the effective conductivity, $K_{\text{eff,SC}}$ is:

$$K_{\text{eff,SC}} = 1/3[p/(2K_{\text{eff,SC}} + K_{\eta}) + (1-p)/(2K_{\text{eff,SC}} + K_{\omega})]^{-1} \quad (21)$$

At $p_{\text{shale}} < 10\%$ and $p_{\text{shale}} > 90\%$, the self-consistent approach provides an excellent approximation of effective conductivity in isotropic periodic media (Fig. 9b). In that range of p_{shale} , K_{eff} of the regular media and $K_{\text{eff,SC}}$ coincide with the upper (if $\kappa < 1$) and lower (if $\kappa > 1$) Hashin–Shtrikman bounds for isotropic binary media [25,14]. Note that K_{eff} of the interlacing media “S-i-2” and “C-i-1” falls outside the Hashin–Shtrikman bounds [$K_{\text{HS,lower}}, K_{\text{HS,upper}}$] for $p_{\omega} > 10\%$ due to the aniso-probable spacing and interlacing of the isotropic inclusions! In the case of sand inclusions, interlacing perpendicular to the flow direction reduces K_{eff} to values below the lower bound, while in the case of clay inclusions, interlacing parallel to the flow direction increases K_{eff} to values above the upper bound (Fig. 9b). This is significantly different from non-interlacing periodic media. For example, Byström [6] compared the two-dimensional K_{eff} of periodic media with random, rectangular (2D Type I EFD), and also hexagonal (2D Type II EFD) arrangement of spherical inclusions with $\kappa > 1$ against the lower Hashin–Shtrikman bound. While the hexago-

nal arrangement gave the lowest K_{eff} among the three arrangements, it was not lower than the Hashin–Shtrikman bound.

If interlacing of isotropic clay/shale inclusions is perpendicular to the mean flow direction (“C-i-2”), $K_{\text{eff,SC}}$ is a good approximation, even at higher p values (up to 58%). However, with sand/sandstone inclusions at $p_{\text{sand}} > 25\%$, $K_{\text{eff,SC}}$ significantly overestimates effective conductivity regardless of the direction of interlacing (“S-i-1” and “S-i-2”).

Self-consistent approximations of effective conductivity, $K_{\text{eff,SC-aniso}}$, in anisotropic media ($R_{bh}, R_{bv}, \lambda_z/\lambda_x \neq 1$) have been presented by Poley [45]. $K_{\text{eff,SC-aniso}}$ for flow parallel and orthogonal to the main anisotropy axis are significantly lower than the observed K_{eff} of the anisotropic ordered media with the clay/shale inclusions (Fig. 9b). On the other hand, $K_{\text{eff,SC-aniso}}$, like $K_{\text{eff,SC}}$, significantly overestimates effective conductivity in ordered media with sand/sandstone inclusions, regardless of anisotropy direction.

5. Conclusion

This paper presents an original solution for the effective conductivity of a binary medium characterized by a regular (periodic) pattern of identically sized cuboid inclusions located on an octahedral lattice. We describe the constitutive geometry \mathcal{G}_{II} and determine the effective conductivity of the macro-domain by determining the flow through the “elementary flow domain” (EFD, Fig. 3), which is an octant of the unitary domain or unit cell of the periodic media.

For the six-dimensional parameter space of $\{\kappa, \mathcal{G}_{\text{II}}\}$, we derive practical bounds of interest. We then and numerically compute solutions for over 14,000 individual parameter combinations spanning the bounded parameter space in regular intervals. Using non-linear interpolation of the numerical results, a continuous solution $K_{\text{eff}}(\kappa, \mathcal{G}_{\text{II}})$ is obtained for the entire parameter space within the limits $10^{-4} < \kappa < 10^4$, $10^{-3} < R_{bh}, R_{bv} < 10^2$, and $1.0667 < L_x, L_y, L_z < 8$.

The results provide the low entropy bounds for the effective conductivity in natural media, which are less ordered than the system considered here. Comparison of the results to effective conductivities derived for random heterogeneous media and to several self-consistent estimates demonstrate similarities and differences in the behavior of the effective conductivity between random and regular media. The following are key conclusions:

- I. The approach allows us to directly compare effective conductivities of very low entropy (regular) media against that of high entropy (random) media over a large range of structural geometries. By comparing measured effective conductivity of

natural media to those of respective random and regular media representations as presented, e.g., in Fig. 9, it may be possible to determine the degree of entropy within the natural media.

- II. The regular media solution developed here allows for consideration of aniso-probable spacings between inclusions, i.e., for media where the probability of encountering an inclusion is not identical in all directions. Because of the aniso-probability condition, the absolute bounds of K_{eff} for isotropic inclusions are the Wiener bounds, not the Hashin-Shtrikman bounds.
- III. For media with large spacing of isotropic, cubic inclusions ($L_x, L_y, L_z > 3$; $p < 0.08$), the results are in agreement with the self-consistent effective conductivity originally proposed by Bruggeman [5] and applied to porous media by Poley [45] and Dagan [14].
- IV. For anisotropic cuboid inclusions, or at relatively close spacing in at least one direction ($p > 0.2$), the effective conductivity of the periodic media is significantly different from that found in anisotropic random binary or Gaussian media:
 - A. Periodic media with low conductivity inclusions have a higher effective conductivity than random binary or log-normal conductivity media with equivalent phase-proportions (or variance) and anisotropy ratio due to the strong connectivity in the higher permeable η -phase.
 - B. Periodic media with high conductivity inclusions have lower effective conductivity than equivalent random or log-normal media due to the isolation of the inclusions. Isolation is not observed in correlated binary random indicator media with $p > 0.13$ due to the existence of the percolation threshold.

The practical applicability of the periodic media approach with aniso-probable and non-stationary K distribution to hydrogeologic problems remains to be investigated. But consider, for example, the structure within alluvial depositional systems of neozoic origin: These systems reflect the depositional regimes of alternate short-term flooding events and longer term non-flooding stages. At a longer time-scale, the depositional system reflects climatic and possibly tectonic cycles, which lead to multiscale hierarchical depositional systems [56]. The solution presented here allows us to explore the effects of multiple scales within a flow system on effective hydraulic conductivity. In its simplest expression of isotropic inclusions, we observe a dichotomy of effective conductivity (“C-i-1” vs. “C-i-2” and “S-i-1” vs. “S-i-2” in Fig. 9) at identical volume proportions, hydraulic conductivity contrasts, and inclusion shape merely due to the intermediate scale non-station-

arity created by interlacing. Future work is needed to further explore such applications.

Acknowledgments

This work has been funded by the University of California Collaborative University-Los Alamos Research Program. Partial funding has also been provided by the Danish Research Agency and The Spanish Nuclear Waste Management Agency (ENRESA). We would like to thank the anonymous reviewers for their constructive comments and support.

Appendix A. Transfer function for $K_{\text{eff}}^*(\kappa, \mathcal{G}_{\text{II}})$ through neural network training

In light of the complexity of the observed parametric relationship $K_{\text{eff}}^*(\kappa, \mathcal{G}_{\text{II}})$ (Figs. 5–8), we chose to use neural network training rather than non-linear multivariate regression to determine a continuous transfer function $K_{\text{eff}}^*(\kappa, \mathcal{G}_{\text{II}})$. The transfer function is obtained by minimizing an objective function based on the difference between $K_{\text{eff}}^*(\kappa, \mathcal{G}_{\text{II}})$ and measured values $K_{\text{eff}}^*(\kappa, \mathcal{G}_{\text{II}})$. We trained a multilayer perceptrons feedforward neural network with sigmoid activation functions (originally due to [49], and discussed at length in most neural network textbooks, e.g., [4]) due to the smooth and generally sigmoidal behavior of $K_{\text{eff}}^*(\kappa, \mathcal{G}_{\text{II}})$. Data input and output are automatically scaled using minimum/maximum and mean/standard deviation linear scaling. The neural network consists of a layered feed-forward topology (input layer, multiple hidden layers, output layer). Optimization is achieved using a combination of backward propagation with time-varying learning rate and momentum and order shuffling in the early stage and a conjugate gradient descent in the final stage with automatic cross verification: After a fit is obtained, the model is tested on a verification set or test set. To take full advantage of the dataset obtained from the MODFLOW simulations, which represents a single sample layer across the parameter space $\{\kappa, \mathcal{G}_{\text{II}}\}$, we apply the bootstrap (bagging) method with random resampling. One third of the input data is randomly picked as verification dataset. Optimization with bagging ensures better global optimization and allows us to simultaneously estimate the predictive capability of the neural network.

Initially, neither the exact number of hidden layers (from 2 to 4) nor the number of units within each layer is specified. The optimal number of hidden layers and layer units is determined with an automatic search algorithm that tests multiple networks and improves network topology based on neural network regularization and sensitivity analysis. Over-fitting of the neural network is suppressed by using a selection data-set and

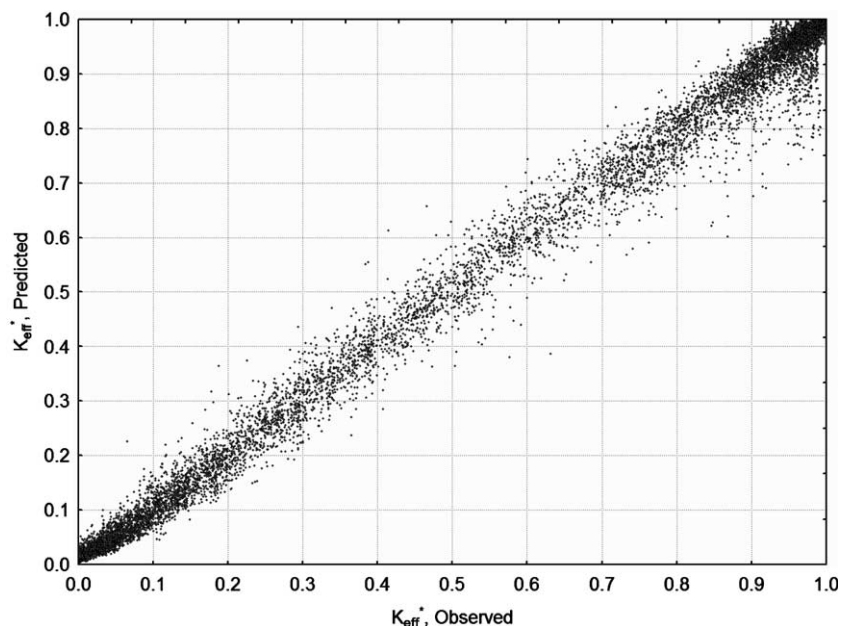


Fig. 10. Predicted vs. observed dimensionless effective conductivity, K_{eff}^* for a trained neural network with two hidden layers in a feed-forward topology. A self-contained program of the neural network transfer function for K_{eff}^* can be obtained from the corresponding author.

by checking error on that set during the iteration process (when the error increases, the optimization terminates). To penalize networks with large curvature (overfitting), Weigend weight regularization [55] is applied, which removes hidden units once all weights are below a given threshold.

The best network training was achieved by limiting the training to the dataset with $0.1 < K_{\text{eff}}^*(\kappa, \mathcal{G}_{\text{II}}) < 0.9$ (approximately 4000 datapoints). The optimal neural network trained on the dataset contained two hidden layers in a 6-35-34-1 topology. The mean absolute error of the network is less than 4% with a correlation coefficient of 99% (Fig. 10). The trained network (available as an easy-to-use black-box DOS program from the corresponding author) represents an empirical continuous upscaling function $K_{\text{eff}}^{*\kappa}(\kappa, \mathcal{G}_{\text{II}})$ for flow in binary media with a Type II EFD. The only limitation is that the parameters of the EFD must be within the limits of $\{\kappa, \mathcal{G}_{\text{II}}\}$ spanned by the training dataset given in Table 1.

References

- [1] Baltean D, Levy T, Balint S. Diffusion-convection in porous medium with impervious inclusions at low flow rates. *Transport Porous Media* 2003;51:19–39.
- [2] Bear J. *Dynamics of fluids in porous media*. New York; 1972.
- [3] Beran MJ. *Statistical continuum physics*. New York; 1968, 424pp.
- [4] Bishop C. *Neural networks for pattern recognition*. Oxford: University Press; 1995.
- [5] Bruggeman DAG. Berechnung verschiedener physikalischer Konstanten von heterogenen Substanzen. *Ann Phys (Leipzig)* 1935;24:636–79.
- [6] Byström J. Influence of the inclusions distribution on the effective properties of heterogeneous media. *Composites Part B* 2003;34:587–92.
- [7] Carle SF, Fogg GE. Transition probability-based indicator geostatistics. *Math Geol* 1996;28(4):453–77.
- [8] Carle SF, Fogg GE. Modeling spatial variability with one- and multi-dimensional continuous Markov chains. *Math Geol* 1997;29(7):891–917.
- [9] Carr JR. Statistical self-affinity, fractal dimension, and geologic interpretation. *Eng Geol* 1997;48:269–82.
- [10] Cushman JH. An introduction to hierarchical porous media. In: Cushman JH, editor. *Dynamics of fluids in hierarchical porous media*. London; 1990. p. 1–6.
- [11] Dagan G. Models of groundwater flow in statistically homogeneous porous formations. *Water Resour Res* 1979;15:47–63.
- [12] Dagan G. Analysis of flow through heterogeneous random aquifers by the method of embedding matrix, 1. Steady flow. *Water Resour Res* 1981;17:107–22.
- [13] Dagan G. Statistical theory of groundwater flow and transport: pore to laboratory, laboratory to formation, and formation to regional scale. *Water Resour Res* 1986;22(9):120S–34S.
- [14] Dagan G. *Flow and transport in porous formations*. Berlin–New York; 1989. 465p.
- [15] Dagan G, Neuman SP. *Subsurface flow and transport: a stochastic approach*. UNESCO, Cambridge University Press; 1997. 241p.
- [16] Dagan G, Lesoff SC. Solute transport in heterogeneous formations of bimodal conductivity distribution, 1. Theory. *Water Resour Res* 2001;37(3):465–72.
- [17] Desbarats AJ. Numerical estimation of effective permeability in sand-shale formations. *Water Resour Res* 1987;23(2):273–86.
- [18] Desbarats AJ. Dispersion in sand-shale sequences. *Water Resour Res* 1990;26(1):153–63.
- [19] Durlofsky LJ. Numerical calculation of equivalent grid block permeability tensors for heterogeneous porous media. *Water Resour Res* 1991;27(5):699–708.
- [20] Dykhne AM. Conductivity of two-dimensional two-phase system. *Sov Phys JETP* 1971;32:63–5.

- [21] Fel LG, Kaganov IV. Relation between effective conductivity and susceptibility of two-component rhombic checkerboard. *J Phys A: Math Gen* 2003;36:5349–58.
- [22] Fisher KD, Stroud D. Conductivity and magnetoresistance of a periodic composite by network discretization. *Phys Rev B* 1997;56(22):14366–73.
- [23] Govindaraju RS, editor. Stochastic methods in subsurface contaminant hydrology. American Society of Civil Engineers; 2002.
- [24] Harbaugh AW, Banta ER, Hill MC, McDonald MG. MODFLOW-2000, The US Geological Survey Modular Ground-Water Model—User Guide to Modularization Concepts and The Ground-Water Flow Process. Open-File Report 00-92, United States Geological Survey, Boulder, CO; 2000. 121p.
- [25] Hashin Z, Shtrikman S. A variational approach to the theory of the effective magnetic permeability of multiohase materials. *J Appl Phys* 1962;33:3125–31.
- [26] Hui L, Ke-da B. Effective conductivity in a checkerboard geometry at high conductance ratio and high concentration. *Phys Rev B* 1992;46(14):9209–12.
- [27] Hsu C-T, Cheng P, Wong KW. A lumped-parameter model for stagnant thermal conductivity of spatially periodic porous media. *J Heat Transfer* 1995;117:264–9.
- [28] Hsu CT. Heat conduction in porous media. In: Vafai K, editor. Handbook of porous media. New York: Dekker; 2000. p. 171–201.
- [29] Journel A, Huijbregts ChJ. Mining geostatistics. Academic Press; 1978. 600p.
- [30] Ke-da B, Axell J, Grimvall G. Electrical conduction in checkerboard geometries. *Phys Rev B* 1990;41(7):4330–3.
- [31] Knudby C, Carrera J. On the relationship between geostatistical, flow, and transport connectivity measures. *Adv Water Resour*, in press.
- [32] Lu S-Y. Effective conductivities of rectangular arrays of aligned spheroids. *J Appl Phys* 1999;85(1):264–9.
- [33] Markov KZ. Elementary micromechanics of heterogeneous media. In: Markov KZ, Preziosi L, editors. Heterogeneous media: micromechanics modeling methods and simulations. Switzerland: Basel; 2000. p. 1–162.
- [34] Markov KZ, Preziosi L, editors. Heterogeneous media: micromechanics modeling methods and simulations. Switzerland: Basel; 2000. 477p.
- [35] McLain DH. Drawing contours from arbitrary data points. *Comput J* 1974;17:318–24.
- [36] Maxwell JC. Treatise on electricity and magnetism, vol. I. 2nd ed.. Oxford: Clarendon Press; 1881. [reprinted by Dover, New York, 1954].
- [37] Miloh T, Benveniste Y. A generalized self-consistent method for the effective conductivity of composites with ellipsoidal inclusions and cracked bodies. *J Appl Phys* 1988;63(3):689–96.
- [38] Milton GW. Bounds on the complex permittivity of a two-component composite material. *J Appl Phys* 1981;52(8):5286–93.
- [39] Milton GW. The theory of composites. United Kingdom: Cambridge; 2002. 719pp.
- [40] Molz FJ, Boman GK. A fractal-based stochastic interpolation scheme in subsurface hydrology. *Water Resour Res* 1993;29:3769–74.
- [41] Molz FJ, Boman GK. Further evidence of fractal structure in hydraulic conductivity distributions. *Geophys Res Lett* 1995;22(18):2545–8.
- [42] Nozad S, Carbonell RG, Whitaker S. Heat conduction in multiphase systems. I: Theory and experiments for two-phase systems. *Chem Eng Sci* 1985;40:843–55.
- [43] Obsonov YV. Periodic heterogeneous structures: new explicit solutions and effective characteristics of refraction of an imposed field. *SIAM J Appl Math* 1999;59(4):1267–87.
- [44] Ochoa-Tapia JA, Stroeve P, Whitaker S. Diffusive transport in two-phase media: Spatially periodic models and Maxwell's theory for isotropic and anisotropic systems. *Chem Eng Sci* 1994;49:709–26.
- [45] Poley AD. Effective permeability and dispersion in locally heterogeneous aquifers. *Water Resour Res* 1988;24(11):1921–6.
- [46] Renard Ph, de Marsily G. Calculating equivalent permeability: a review. *Adv Water Res* 1997;20(5–6):253–78.
- [47] Renault P. The effect of spatially correlated blocking-up of some bonds or nodes of a network on the percolation threshold. *Transport Porous Media* 1991;6:451–68.
- [48] Roberson JA, Crowe CT. Engineering fluid mechanics. John Wiley and Sons; 1997. 698p.
- [49] Rumelhart DE, McClelland J, editors. Parallel distributed processing, vol. 1. Cambridge, MA: MIT Press; 1986.
- [50] Sahimi M. Applications of percolation theory. London, Great Britain; 1994. 258p.
- [51] Sahimi M. Fractal-wavelet neural-network approach to characterization and upscaling of fractured reservoirs. *Comput Geosci* 2000;26:877–905.
- [52] Statsoft, Inc. STATISTICA 6.0, Tulsa, OK; 2002.
- [53] Torquato S. Random heterogeneous media: microstructure and macroscopic properties. Berlin; 2001. 712pp.
- [54] Vogel H-J, Roth K. Moving through scales of flow and transport in soil. *J Hydrol* 2003;272:95–106.
- [55] Weigand AS, Rumelhart DE, Huberman BA. Generalization by weight-elimination with application to forecasting. In: Lippmann RP, Moody JE, Touretzky DS, editors. Advances in neural information processing systems, vol. 3. San Mateo, CA: Morgan Kaufmann; 1991. p. 875–82.
- [56] Weissmann GS, Carle SF, Fogg GE. Three-dimensional hydrofacies modeling based on soil surveys and transition probability geostatistics. *Water Resour Res* 1999;35(6):1761–70.
- [57] Wiener O. Abhandlungen der Mathematischen-Physischen Klasse der Königlich Sächsischen Gesellschaft der Wissenschaften 1912;32:509.
- [58] Wheatcraft SW, Tyler SW. An explanation of scale-dependent dispersivity in heterogeneous aquifers using concepts of fractal geometry. *Water Resour Res* 1988;24(4):566–78.
- [59] Whitaker S. The method of volume averaging. The Netherlands: Dordrecht; 1999. 217p.
- [60] Wu J, Hu BX, Zhang D, Shirly C. A three-dimensional numerical method of moments for groundwater flow and solute transport in a nonstationary conductivity field. *Adv Water Resour* 2003;26:1149–69.
- [61] Yao K, Habibiyan MT, O'Melia CR. Water and wastewater filtration: concepts and application. *Environ Sci Technol* 1971;5(11):1105–12.
- [62] Yeo I-W, Zimmerman RW. Accuracy of the renormalization method for computing effective conductivities of heterogeneous media. *Transport Porous Media* 2001;45:129–38.
- [63] Zehner P, Schlunder EU. Thermal conductivity of granular materials at moderate temperatures. *Chem Ing Technol* 1970;42:933–41.